# An approach to optimal integer and fractional-order modeling of electro-injectors in compression-ignition engines

Paolo Lino[a], Guido Maione[a], Roberto Garrappa[b], Sverre Holm[c]

[a]Dept. of Electrical & Information Engineering, Polytechnic University of Bari, Italy
[b]Department of Mathematics, University of Bari, Italy
[c]Department of Physics, University of Oslo, Norway

## Abstract

The automotive industry continuously spends resources to reduce fuel consumption, operating costs, and harmful emissions. Namely, regulations are becoming more restrictive and customers' expectations are growing. To achieve these goals in compression-ignition engines, an approach employs innovative Common Rail Injection Systems, based on advanced control units and electro-injectors. The latter require an accurate model for optimizing layout and operation and for controlling injection rate shaping strategies that are fundamental for reducing consumption and emission. This work proposes a complete innovative electro-injector model, which integrates an integer-order representation of inner volumes and mechanical and electromagnetic elements, and a fractional-order model for the high-pressure fuel propagation inside a specific pipe in the injector. Fractional-order modeling of this complex process is motivated by the superior description ability of a fractional-order system with respect to an integer-order system. Then a

*Email addresses:* paolo.lino@poliba.it (Paolo Lino), guido.maione@poliba.it (Guido Maione), roberto.garrappa@dm.uniba.it (Roberto Garrappa), sverre.holm@fys.uio.no (Sverre Holm)

This paper is published in *Control Engineering Practice*, Vol. 115, Oct. 2021, 104890, https://doi.org/10.1016/j.conengprac.2021.104890.

new numerical method is proposed and tuned to simulate the system. A differential evolution technique optimizes the model parameters. Simulation results show that benefits are gained in model prediction capability.
*Keywords:*
Fractional calculus, fractional-order modeling, common rail diesel engine, electro-injector.

## 1. Introduction

In the last decade, injection systems of automotive engines improved their performance due to consistent technology advancements. The continuous assessment of restrictions by national and international regulations, and the demand for a lower environmental and economical impact, which is made possible by alternative fuels and electric or hybrid engines, are further stimulating research in this field.

In case of compression-ignition engines, many efforts have been based on the common rail (CR) technology to achieve lower fuel consumption and reduce emission of polluting gases and particulate matters [33]. In CR injection systems (Fig. 1), a properly filled CR volume and electronically driven injectors are combined to obtain a more accurate metering of the ratio between air and fuel and a better combustion process [33]. In this way, a suitable engine performance and lower emission is guaranteed with varying engine speed and applied load, whichever are the operating conditions [15, 11, 19, 36].

Control is twofold. Firstly, the injection timing must be precisely adjusted to let the proper amount and rate of fuel enter the combustion chamber. To this aim, electro-injectors opening time interval is ruled according to the required speed and

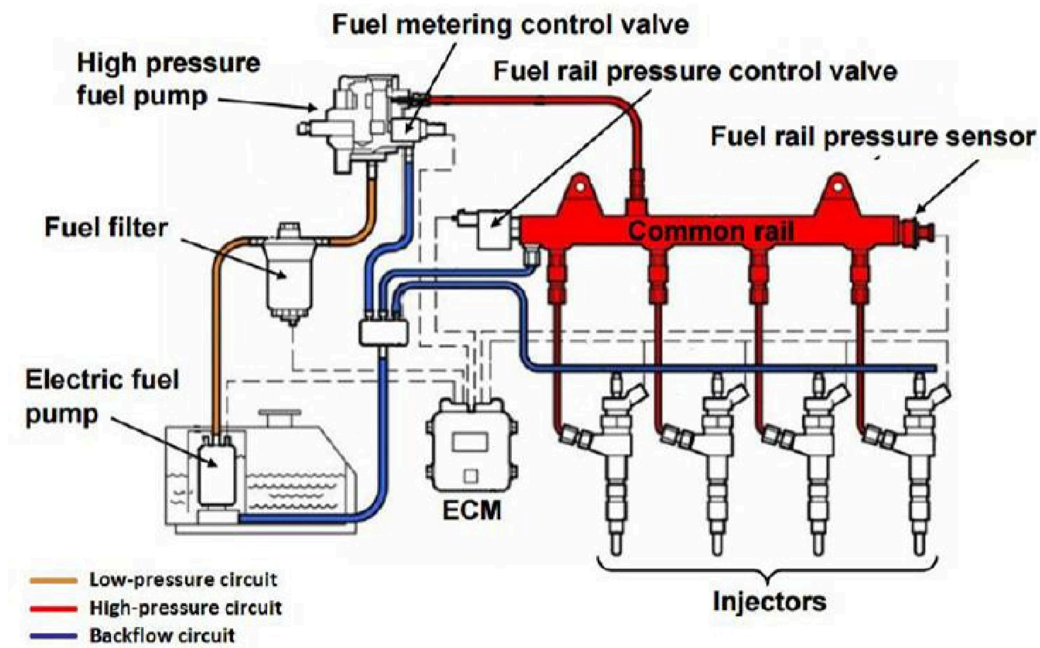


Figure 1: Common Rail injection system

applied load. Secondly, the fuel injection pressure in the CR volume is regulated. In both cases, an electronic control module (ECM) can implement any control algorithm efficiently. A common approach to command injection is to compute and organize reference values of CR pressure and injectors timing in special maps (e.g. lookup tables). With reference to Fig. 1 (with injectors of amplified size), the ECM accurately meters the air-fuel ratio and shapes the injected flowrate by adjusting the injectors timing and regulating the CR fuel pressure at required reference levels.

An accurate representation of the injection system is important to solve the two control problems and improve model-based control strategies. In detail, advanced electro-injectors play a strategic role to obtain suitable injection flowrate shaping (IRS). However, since optimizing IRS by experiments is complex and time-consuming, the model-based approach often turns out more convenient [22, 21, 23].

This paper focuses on modeling an innovative electro-injector for Diesel CR engines in the most typical operating conditions. The effort is to better describe certain fluid-dynamic processes associated with the high-pressure fuel flow according to wave propagation. However, the model should be tractable for prediction and control. To this aim, the most important components (mechanical and electromagnetic elements, accumulation volumes, a pipe delivering the fuel from the CR volume) and physical phenomena (mechanical deformation, fuel flow and propagation, viscosity) are considered only. The fuel dynamics in the characteristic pipe is represented by a fractional-order model, which is motivated by starting from the Navier-Stokes equations and using fractional viscosity. The presented set of partial differential equations (PDEs) with time derivatives of fractional-order preserves conservation laws thanks to a physical interpretation of the fractional model.

It is not the first time that fractional models and controls are applied to automotive engineering. A non-integer-order controller of the air path in a Diesel engine was designed in [7], but with no emphasis on the fuel flow. In [26], the authors show the non-integer-order control of the air/fuel ratio in internal combustion engines. In [21, 22, 23], fractional control of CR pressure in gas engines is applied to an integer-order model, but the fluid is compressible and viscosity is not considered. In [18], simplified fractional transfer functions are given for the whole injection system, with no attention to fuel dynamics. Here, for the first time and to the best of authors' knowledge, the focus is on the specific viscous fuel dynamics inside the injector and on wave propagation phenomena, such that the dynamics is represented by fractional partial differential equations. The model parameters are calibrated by a simulation-optimization approach, which employs differential evolution and a performance index based on the injected flowrate prediction error. The results from the optimized model are compared to available data from a real injector.

In the following, Section 2 introduces the electro-injector. Section 3 provides the mathematical model of all parts not requiring fractional calculus. Section 4 justifies the fractional model for fuel propagation. Section 5 presents the numerical method for simulation. Section 6 establishes the optimization problem that is then solved by differential evolution. Sections 7 and 8 show the simulation results and provide the conclusions.

## 2. System description

This work considers a prototype electro-injector of new generation that is employed in Diesel CR injection systems [2, 25]. Similar studies characterized microfluidic systems, but fluids were treated as incompressible, multiphase (two fluids are interacting), with dispersion of droplets, and the analysis is especially oriented to bubble flow dynamics control through microchannels [29, 1, 5, 4, 12, 13]. Herein, difficulty arises from the complex high-pressure fuel flow in the tiny volumes of the injector, through small orifices and along different flow paths. In particular, a pipe connects the injector input, which supplies fuel coming from the CR volume, to a volume in which fuel is accumulated before injection. Nonlinear fuel dynamics and mechanical deformation of relevant parts must be represented.

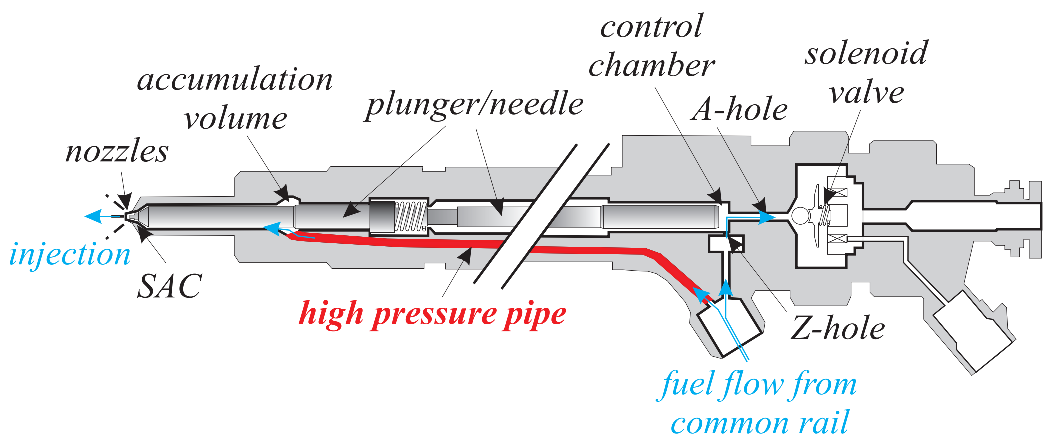


Figure 2: Scheme of electro-injector

To this aim, the scheme in Fig. 2 is useful: the electro-injector is shown horizontally for sake of clarity and that a cross-cut reduces the picture.

Fuel flows in the injector by a *control path* and a *feeding path*. In the first path, fuel passes through a Z-hole (a pipe with a very tiny section), a control chamber with variable size, a A-hole, and finally a low pressure zone. The section of entrance into this zone is varied by a shutter of an electro-hydraulic solenoid valve driven by a PWM voltage. In the second path, fuel from the CR passes through a high pressure pipe, an accumulation volume, a SAC (from *cul-de-sac*) volume, and finally the nozzles. In both paths, fuel flows at high pressure. The most peculiar element is the narrow pipe linking the CR and accumulation volume. Namely, the fuel flow is subject to high-frequency variations because the input pressure to this pipe (i.e. the pressure in the CR) is subject to abrupt changes by the solenoid valve commands to the control circuit.

Moreover, fuel flow is regulated by a plunger-needle element that is made of several cylinders of different sections, connected to each other. If the needle moves up, the accumulation volume gets connected to the SAC volume and fuel outflows. The lift depends on the difference of pressures in the control chamber and accumulation volume, say $(p_{CC} - p_{AV})$, such that the injector can be opened (closed) by reducing (increasing) $p_{CC}$. If the solenoid valve is opened (shutter up), $p_{CC}$ diminishes because fuel can enter the low pressure zone and the plunger-needle coupling is pushed up (from left to right in Fig. 2). If the valve is closed (shutter down), $p_{CC}$ increases, as the CR pressure pushes down the plunger-needle coupling (from right to left in Fig. 2).

To synthesize, the fuel dynamics is determined by various factors. Injection events determine the nonuniform distribution of pressure in the CR volume. Moreover, fast, multiple and close injections cause a water hammer effect in the injector. The flow in the injector also depends on the employed fuel, elastic deformation of pipes, distributed friction losses and damping because of viscosity effects.

The following two sections provide a mathematical model of all relevant dynamics and elements. Integer-order, lumped parameters representations are usually used, but a distributed parameters model is necessary for the high pressure pipe, in which wave propagation of pressure can be experimentally observed.

## 3. Integer-order modelingof the electro-injector

The model represents the injector as a set of interconnected volumes drawn within a finite region of the flow, i.e. the control chamber, the accumulation volume, and the SAC volume. Each volume is sufficiently small to assume uniform physical properties of the fuel. Pressure is different in each volume. The continuity equation, the momentum equation, the Newton's second law, the Faraday's law and other laws are applied to each volume and the crossing surfaces. Ordinary differential equations (lumped parameters) model those parts in which pressure is uniform and time-varying. Instead, in presence of non-stationary flows, PDEs (distributed parameters) describe wave propagation in the tubes. Modeling the high pressure pipe as a unique volume inhibits a correct representation of the propagation of pressure waves, and a proper characterization of losses and propagation delays. Therefore, a set of nonlinear PDEsrepresents the flow in the pipe. Finally, parameters change with pressure (not with temperature) and elastic deformation of the moving parts and cavitation through the holes are considered.

### *3.1. Representation of control volumes*

Fuel thermodynamic properties vary with operating conditions. For pressures between 0.1 and 200 MPa and temperatures between 10 and 120 °C, fuel density $\rho$, kinematic viscosity $\nu$, dynamic viscosity $\eta$, bulk modulus $K_f$, and speed of sound in the fluid are assumed dependent on the instantaneous pressure $p$ inside each volume [10]:

$$\begin{cases} \rho(p,\bar{T}) = K_{\rho 1} + [1 - e^{-p/K_{\rho 2}}]\, K_{\rho 3}\, p^{K_{\rho 4}} \\ \nu(p,\bar{T}) = K_{\nu 1} + K_{\nu 2}\, p^{K_{\nu 3}} \\ \eta(p,\bar{T}) = \nu(p,\bar{T})\, \rho(p,\bar{T}) \\ K_f(p,\bar{T}) = K_{B1} + [1 - e^{-p/K_{B2}}]\, K_{B3}\, p^{K_{B4}} \\ c(p,\bar{T}) = \sqrt{K_f(p,\bar{T})/\rho(p,\bar{T})} \end{cases} \tag{1}$$

where $K_{\rho i}$, $K_{Bi}$, $K_{\nu i}$ are polynomial functions of the temperature $\bar{T}$. If a reliable measure of $\bar{T}$ is not available, then $\bar{T} = 80\,°\mathrm{C}$ is considered. The assumptions in (1) improve the prediction achieved by constant parameters or linear functions [24].

Moreover, since the fuel is compressible, the bulk modulus is used in the following equation:

$$\frac{dp}{dt} = -\frac{K_f}{V}\left(\frac{dV}{dt} - Q_{leak} + \sum_i Q_i\right) \tag{2}$$

where the fluid volume $V$ changes because of movement of the plunger-needle coupling, $Q_{leak}$ is the leakage flowrate between coupled mechanical elements in relative motion while being lubricated by the fuel, specified as in [32], and $\sum_i Q_i$ is the algebraic sum of intake and outtake flowrates, which are specified as in [20]. Integration of (2) gives $p$ provided that flowrates, instantaneous volumes, and initial conditions are available.

In particular, for the accumulation volume, pressure $p_{AV}$ is obtained by neglecting $Q_{leak}$ and by $Q_i = u_i\, A_i$, where $u_i$ are the velocities and $A_i$ are the areas of sections [28]. This pressure will be useful as boundary condition to solve the continuity and momentum equations for the high pressure pipe: namely, $p_{AV}$ is the pressure at the outlet section of the pipe.

### *3.2. Computation of flow sections*

Flow sections are changed by valve operation or by deformation of mechanical elements. In detail, $h_{ev}$ indicates the displacement of the valve shutter that changes section $A_{0,ev}$ of the A-hole; $h_{SAC}$ indicates the displacement of the plunger-needle coupling that changes the section $A_{0,SAC}$ between the accumulation and SAC volumes. The main relation is:

$$A_0 = \frac{\pi}{2}\,\left[2\, d_m + h\, \sin(2\theta)\right]\, h\, \sin(\theta) \tag{3}$$

where $d_m$ is the minimum sealing diameter, $\theta$ is the angle formed by the seat, $h$ is $h_{ev}$ or $h_{SAC}$ and $A_0$ is $A_{0,ev}$ or $A_{0,SAC}$, respectively [19].

Actually, the injected flowrate depends on the axial position of the needle tip, which in its turn changes by the plunger-needle deformation caused by high pressure. The reduction of the axial length of the coupling increases the flow section below the needle tip, i.e. $A_{0,SAC}$, which is nonlinearly depending on the pressure on the mechanical parts.

### *3.3. Representation of mechanical elements*

The plunger-needle coupling can be represented as a mass-spring-damper system. The two elements are a series of five and two elementary cylinders, respectively, each being characterized by a different section and mass ($m_i$ for $i = 1, \ldots, 7$). Then, every intermediate element in the model includes halves of the masses of two adjacent cylinders, except for the first and last elements in the chain including one-half of the mass of the first and last cylinders, respectively (Fig. 3). The masses are linked by spring and damping elements, and the plunger-needle connection is by a spring representing the contact force.

The main problem is to determine the optimal parameters that fitthe experimental injected flowrate. A free-body equation can be derived by applying Newton's second law to each mass $M_i$ of the mass-spring-damper model:

$$\begin{aligned} M_i\ddot{z}_i + c_{i-1}(\dot{z}_i - \dot{z}_{i-1}) + c_i(\dot{z}_i - \dot{z}_{i+1}) \\ + k_{i-1}(z_i - z_{i-1}) + k_i(z_i - z_{i+1}) = \sum_i F_i, \end{aligned} \tag{4}$$

where $z_i$ is the deformation of the mass element, $c_i$ is the damping coefficient, $k_i$ is the elastic constant of the elements located between each mass, and $\sum_i F_i$ is the resultant of pressure forces on the half modeled cylinder. The spring constant is $k_i = E \cdot A_i/l_{0i}$, where $E$ is the Young's modulus, $A_i$ is the cross section area of the considered cylinder, and $l_{0i}$ is the initial length of the element. The values of the spring constants computed by this way are shown in Table 1 and are used as initial values for the parametric optimization shown in Section 6.The damping coefficient is $c_i = 2\,\xi\,\sqrt{k_i \cdot M_i}$, with $\xi = 0.005$ [10], which simplifies the parameters optimization.

The injection flowrate $Q_i$ is a nonlinear function of the needle displacement (then of the flow section), which equals $z_9$ of mass $M_9$ in Fig. 3. Given that a constant discharge coefficient $c_d$ does not accurately model how deformation affects the injection flow and distinguish different injection phases, the variation of $c_d$ is considered as follows [10]. At the beginning of the opening phase, $c_d$ increases up to $c_d(z_0)$. Subsequently, a linear dependence establishes up to $c_d(z_M)$. Finally, $c_d = c_d(z_M)$ during the closing transient. Note that $z_0 = K_3\,p_{CR} + K_4$ and $z_M = K_1\,p_{CR} + K_2$ (maximum needle lift), where $p_{CR}$ is the CR pressure. The constant parameters $K_1$, $K_2$, $K_3$, $K_4$, $c_d(z_0)$, $c_d(z_M)$ must be experimentally determined.

The resulting mechanical equations are:

$$
\begin{cases}
M_1\ddot{z}_1 + c_1\dot{z}_1 + k_1 z_1 = F_1 \\
M_2\ddot{z}_2 + c_1(\dot{z}_2 - \dot{z}_1) + c_2(\dot{z}_2 - \dot{z}_3) \\
\qquad + k_1(z_2 - z_1) + k_2(z_2 - z_3) = F_2 \\
M_3\ddot{z}_3 + c_2(\dot{z}_3 - \dot{z}_2) + c_3(\dot{z}_3 - \dot{z}_4) \\
\qquad + k_2(z_3 - z_2) + k_3(z_3 - z_4) = F_3 \\
M_4\ddot{z}_4 + c_3(\dot{z}_4 - \dot{z}_3) + c_4(\dot{z}_4 - \dot{z}_5) \\
\qquad + k_3(z_4 - z_3) + k_4(z_4 - z_5) = F_4 \\
M_5\ddot{z}_5 + c_4(\dot{z}_5 - \dot{z}_4) + c_5(\dot{z}_5 - \dot{z}_6) \\
\qquad + k_4(z_5 - z_4) + k_5(z_5 - z_6) = F_5 \\
M_6\ddot{z}_6 + c_5(\dot{z}_6 - \dot{z}_5) + k_5(z_6 - z_5) + k(z_6 - z_7) = F_6 \\
M_7\ddot{z}_7 + c_6(\dot{z}_7 - \dot{z}_8) + k_6(z_7 - z_8) + k(z_7 - z_6) = F_7 \\
M_8\ddot{z}_8 + c_6(\dot{z}_8 - \dot{z}_7) + c_7(\dot{z}_8 - \dot{z}_9) \\
\qquad + k_6(z_8 - z_7) + k_7(z_8 - z_9) = F_8 \\
M_9\ddot{z}_9 + c_7(\dot{z}_9 - \dot{z}_8) + k_7(z_9 - z_8) = F_9
\end{cases}
\tag{5}
$$

where $k$ is the fixed elastic constant of the link between the plunger and the needle, and $F_1, ..., F_7$ are the resultant applied pressure forces. The elastic constants $k_1, ..., k_7$ are optimized (see Tab. 1) and the damping coefficients $c_1, ..., c_7$ are determined by $c_i = 0.01\sqrt{k_i \cdot M_i}$ with the optimized values of $k_i$.

The solution of (5) gives $z \equiv z_9$, which depends on the acting pressures, the pressure $p_{CR}$ and the valve operation, and changes the outflow section from the SAC volume to the nozzles, hence determines the closing/opening of the injector.

Table 1: Initial parameters (before optimization) and optimal parameters of the plunger-needle coupling (with integer-order (IO) and fractional-order (FO) model) and of $\alpha$ and $\beta$. Elastic constants are in N/m.

| Element | Par. | In. Val. | Opt. Val. (IO) | Opt. Val. (FO) |
|---|---|---|---|---|
| Plunger | $k_1$ | $1.22 \cdot 10^8$ | $1.50 \cdot 10^8$ | $1.44 \cdot 10^8$ |
| | $k_2$ | $8.08 \cdot 10^7$ | $9.53 \cdot 10^7$ | $6.21 \cdot 10^7$ |
| | $k_3$ | $8.21 \cdot 10^7$ | $7.91 \cdot 10^7$ | $8.62 \cdot 10^7$ |
| | $k_4$ | $9.44 \cdot 10^7$ | $1.37 \cdot 10^8$ | $1.23 \cdot 10^8$ |
| | $k_5$ | $9.43 \cdot 10^7$ | $1.40 \cdot 10^8$ | $1.01 \cdot 10^8$ |
| Needle | $k_6$ | $1.86 \cdot 10^8$ | $3.49 \cdot 10^8$ | $3.50 \cdot 10^8$ |
| | $k_7$ | $5.82 \cdot 10^7$ | $5.80 \cdot 10^7$ | $7.68 \cdot 10^7$ |
| Pipe | $\alpha$ | 1 | 1 | 0.975 |
| | $\beta$ | 1 | 1 | 0.9 |

### *3.4. Representation of valve*

The valve regulates the fuel flow between the control chamber and the low-pressure zone. The valve shutter is linked to a magnet anchor and its position $h_{ev}$ is given by Newton's second law and the applied forces: pressure forces from the hydraulic model and the electro-magnetic force.

The Faraday's law gives the magnetic flux $\varphi$ within the whole magnetic circuit, with $N_{ev}\,\dot{\varphi} = v_{ev} - R_{ev}\,i_{ev}$, where $R_{ev}$ is the coil resistance with $N_{ev}$ turns, $v_{ev}$ the applied voltage and $i_{ev}$ the drawn current. The flux leakage and eddy-currents are neglected. The drawn current comes from the magnetomotive-force that produces the magnetic flux:

$$i_{ev} = \frac{1}{N_{ev}}\,H_a\,l_a + \frac{1}{N_{ev}}\,H_s\,l_s \tag{6}$$

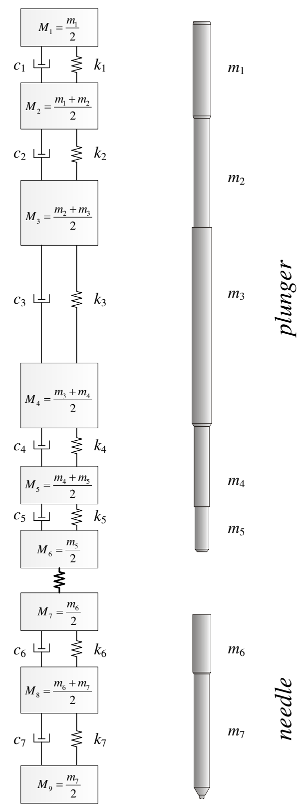


Figure 3: Model of the plunger-needle coupling

where $H_a$, $H_s$, $l_a$, and $l_s$ are the magnetic field strengths and the flow path lengths in the air gap and steel, respectively: $l_s \approx const$, $l_a$ depends on the anchor instantaneous position. If the magnetic flux cross section is assumed constant along the circuit, then $H_a = \varphi/(\mu_0\, A_g)$ and $H_s = f_h(\varphi/A_g)$: $A_g$ is the air gap cross section and $\mu_0$ is the air magnetic permeability. The nonlinear function $f_h$ directly relates to the magnetization curve of the material. The state equation for the magnetic flux is:

$$\dot{\varphi} = \frac{1}{N_{ev}}\, v_{ev} - \frac{R_{ev}}{N_{ev}^2\, \mu_0\, A_g}\, \varphi\, l_a - \frac{R_{ev}}{N_{ev}^2}\, f\left(\frac{\varphi}{A_g}\right)\, l_s \tag{7}$$

and the electromagnetic force is $F_{ev} = \varphi^2/(2\,\mu_0\,A_g)$.

## 4. Fractional-order modeling of the high pressure pipe

The non-stationary flow in the high pressure pipe can be represented by a fractional-order model, as many fluids show hereditary dependencies of power type [34]. This can be demonstrated by starting from a conventional integer-order model.

Let the pressure and the density be composed of a static value plus a perturbation which will be considered to be small:

$$
\begin{aligned}
p' &= p_0 + p, \\
\rho' &= \rho_0 + \rho
\end{aligned}
\tag{8}
$$

Moreover, let the particle velocity be denoted by $u$ and the particle displacement by $s$, where $u = \frac{\partial s}{\partial t}$. Note that these variables and notations are different from the previous terminology.

### 4.1. First fractional model

A first fractional-order model is proposed here starting from the conventional integer-order model based on continuity and momentum equations.

#### 4.1.1. Continuity and momentum equations

The conservation of mass principle is expressed in the equation of continuity. It states that the net influx of matter into a volume element is reflected in a change of density. Under the assumption of small perturbations, the linearized version is:

$$
\frac{\partial \rho}{\partial t} + \rho_0\,\nabla \cdot \overrightarrow{u} = 0. \tag{9}
$$

The linearized constitutive equation is:

$$p = K\,\frac{\rho}{\rho_0},\;\; K = \gamma\, p_0. \tag{10}$$

Combining (9) and (10) gives:

$$\frac{\partial p}{\partial t} + K\,\nabla\cdot\overrightarrow{u} = \frac{\partial p}{\partial t} + c_0^2\,\rho_0\,\nabla\cdot\overrightarrow{u} = 0. \tag{11}$$

The latter equality is based on the speed of sound $c_0^2 = K/\rho_0$.

Navier-Stokes equation in the case of an incompressible fluid and after linearization is

$$\rho_0\frac{\partial\overrightarrow{u}}{\partial t} + \nabla p = \eta\,\nabla^2\overrightarrow{u}. \tag{12}$$

where $\eta$ is the dynamic viscosity in this linearized equation.

### *4.1.2. Validity of Linearization*

A fuel injection system could be one with rapid movement and violent motion. Then one might question the validity of the assumption of small density, pressure and velocity deviations which are the basis for the linearized momentum and mass balances, as well as the linear constitutive law.

For instance, in nonlinear acoustics – of importance both in underwater acoustics and medical ultrasound – one can only linearize the conservation of momentum, but not the equation of state nor the conservation of mass equation.

Pressures inside the injection system vary between 1 and 2000 bars. The modeled pipe connects the feeding CR volume and the accumulation volume. The CR pressure slightly varies during injection, namely the CR volume is large and stores fuel at a pressure between 1000 and 2000 bar (depending on the operating conditions set by the load and driver's needs). In the accumulation volume, fuel pressure drops when the injector opens: it decreases from the CR pressure to a very low value (the accumulation volume is connected to output nozzles by a short pipe, injecting fuel to a pressure which is no more than 10 bar). Very fast opening and closing transients of the injector are observed, while the phase during which the injector is completely open, resulting in flow stationary conditions, is much longer and characterized by an almost constant pressure difference $(\Delta p)$ between the entrance and the exit of the pipe. In conclusion, linearization is acceptable.

#### *4.1.3. From integer- to fractional-order models*

Putting together the previous developments, and considering only the 1-D case, the propagation of pressure waves from the pipe inlet section to the accumulation volume can be represented by the following integer-order continuity and momentum equations:

$$\begin{cases} \dfrac{\partial p}{\partial t} + c_0^2\,\rho_0\,\dfrac{\partial u}{\partial x} = 0 \\ \dfrac{\partial u}{\partial t} + \dfrac{1}{\rho_0}\,\dfrac{\partial p}{\partial x} - \nu\,\dfrac{\partial^2 u}{\partial x^2} = 0 \end{cases} \tag{13}$$

where $\nu = \eta/\rho_0$ is the kinematic viscosity in the presented, linearized model.

Since several fluids show properties expressed by power laws [34], use of non-integer-order time derivatives can be assumed. Namely, the fuel flow in the high pressure pipe does not give a clear experimental evidence of fractional dynamics. However, the proposed fractional-order model could provide better fitting to experimental data, as shown by very interesting results obtained in Section 7. Then the continuity and momentum equations are proposed in a fractional version as

$$\begin{cases} \dfrac{\partial^\alpha p}{\partial t^\alpha} + c_0^2\rho_0\dfrac{\partial u}{\partial x} = 0 \\ \\ \dfrac{\partial^\beta u}{\partial t^\beta} + \dfrac{1}{\rho_0}\dfrac{\partial p}{\partial x} = \nu\dfrac{\partial^2 u}{\partial x^2} \end{cases} \tag{14}$$

where $\alpha, \beta \in (0, 1]$. Typical values of the fractional orders, which were considered in previous analysis, are $\alpha = 0.8, 0.85, 0.9, 0.95, 1$ and $\beta = 0.8, 0.85, 0.9, 0.95, 1$ [14].

These equations can be numerically solved by using boundary conditions, i.e. the instantaneous pressures and flows at the pipe inlet and outlet sections. The inlet pressure is practically given by $p_{CR}$, which is always available by measurements, while the outlet pressure is $p_{AV}$, which is given by integration of (2).

The equations will be analyzed by finding the corresponding wave equation.

#### *4.1.4. Wave equation of the first model*

Apply the operator $\partial^{-\alpha}/\partial t^{-\alpha}$ and then $\partial/\partial x$ on the first equation in (14). Then solve for $\partial p/\partial x$ from the second equation in (14) and eliminate it. The result after application of $\partial^{\alpha}/\partial t^{\alpha}$ is

$$\frac{\partial^2 u}{\partial x^2} - \frac{\rho_0}{K}\frac{\partial^{\alpha+\beta} u}{\partial t^{\alpha+\beta}} + \frac{\eta}{K}\frac{\partial^{\alpha}}{\partial t^{\alpha}}\frac{\partial^2 u}{\partial x^2} = 0. \tag{15}$$

The wave equation is valid for the particle displacement $s$ as well. However, the expressions of (14) are preferred because it is easier to integrate them numerically.

### *4.2. Second alternative fractional model*

Now an alternative fractional model is proposed on the basis of fractional viscosity of the fluid. Start with the linearized equation of continuity in 1-D from (9) and integrate it in time, by replacing velocity $u$ by displacement $s$:

$$\rho + \rho_0\frac{\partial s}{\partial x} = 0. \tag{16}$$

The linearized momentum equation (Euler's equation), which is (12) without viscosity, is:

$$\rho_0\frac{\partial u}{\partial t} + \frac{\partial p}{\partial x} = \rho_0\frac{\partial^2 s}{\partial t^2} + \frac{\partial p}{\partial x} = 0. \tag{17}$$

The equation of state including viscosity is:

$$p = K\frac{\rho}{\rho_0} + \frac{\eta}{\rho_0}\frac{\partial \rho}{\partial t}. \tag{18}$$

#### 4.2.1. Wave equation of the second model

Use (16) to eliminate $\rho$ in (18) giving:

$$p = -K\frac{\partial s}{\partial x} - \eta\frac{\partial}{\partial t}\frac{\partial s}{\partial x}. \tag{19}$$

Then insert that into (17) after spatial integration. The result is:

$$\frac{\partial^2 s}{\partial x^2} - \frac{\rho_0}{K}\frac{\partial^2 s}{\partial t^2} + \frac{\eta}{K}\frac{\partial}{\partial t}\frac{\partial^2 s}{\partial x^2} = 0. \tag{20}$$

This is the viscous wave equation [30].

#### 4.2.2. Fractional version

A fractional continuity or conservation of mass can now be justified. In the non-relativistic and non-fractional case, $E = mc^2$, so it represents conservation of energy in a closed system. In this application, energy which is dissipated will draw energy from the flow and is lost as e.g. heat. It is not converted back into flow again. So this system is not closed as the conservation of energy principle says. The new equation from (16) is:

$$\frac{\partial^{\gamma-1}\rho}{\partial t^{\gamma-1}} + \rho_0\frac{\partial s}{\partial x} = 0,\ 0 < \gamma \leq 1 \tag{21}$$

or

$$\frac{\partial^{\gamma}\rho}{\partial t^{\gamma}} + \rho_0\frac{\partial u}{\partial x} = 0 \tag{22}$$

which shows some similarity with the first equation in (14). However, one equation is concerned with $\rho$ and the other with $p$, and since their relationship is rather complex, see (24), they are less similar than it seems.

The second one, fractional conservation of momentum, i.e. the second equation in (14), is harder to justify. Therefore, we let it stay as it is in the non-fractional form of (17):

$$\rho_0 \frac{\partial^2 s}{\partial t^2} + \frac{\partial p}{\partial x} = \rho_0 \frac{\partial u}{\partial t} + \frac{\partial p}{\partial x} = 0. \tag{23}$$

It is easier to justify a fractional viscosity. This is a property of the gas which is flowing, rather than a characterization of the momentum balance. That means introducing a time fractional term in (18):

$$p = K\frac{\rho}{\rho_0} + \frac{\eta}{\rho_0}\frac{\partial^\alpha \rho}{\partial t^\alpha},\ 0 < \alpha < 1. \tag{24}$$

Going through the same procedure as in the previous section for finding the wave equation gives:

$$\frac{\partial^2 s}{\partial x^2} - \frac{\rho_0}{K}\frac{\partial^{\gamma+1} s}{\partial t^{\gamma+1}} + \frac{\eta}{K}\frac{\partial^\alpha}{\partial t^\alpha}\frac{\partial^2 s}{\partial x^2} = 0. \tag{25}$$

This equation is also derived in Chap. 6 of [16]. Note that as $\gamma$ and $\alpha$ approach unity, i.e. the non-fractional case, this is a fractional extension of the viscous wave equation of (20) [17].

### *4.2.3. Comparison with the first fractional model*

Given that the wave equations capture the totality of this problem, then a comparison of them should give all the information that is required.

Denoting the $\alpha$ and $\beta$ values of the original formulation of (14) as $\alpha'$ and $\beta'$, and using the similarity between (15) and (25) gives:

$$\alpha = \alpha', \gamma = \alpha' + \beta' - 1 \tag{26}$$

and with the range previously found [14], the range of $\gamma$ will be from $0.6$ when $\alpha' = \beta' = 0.8$ to $1$ when $\alpha' = \beta' = 1$. This looks reasonable.

Two final remarks are in order.

**Remark 1.** At the injector working pressures, heat dissipation could be substantial. Moreover, fuel flows in the narrow high pressure pipe inside the injector, so that friction has a certain influence on it. A fractional conservation of mass relates to conservation of energy, and since energy is leaking out of the system, the fractional mass conservation can be justified.

**Remark 2.** It is much harder to justify a fractional momentum balance. As an alternative, the fractional viscosity in the fluid was proposed. It is easier to justify and the solution of the associated equation was analyzed. Moreover, it was found that there is a simple one-to-one relation between the fractional orders of the first model and the second alternative model.

## 5. Numerical Approximation

The absence of analytical solutions in closed form pushes us to adopt a numerical procedure to solve and simulate the system of time–fractional PDEs (14).

To minimize the computational complexity, we discretize time–fractional derivatives in (14) by a standard Grünwald–Letnikov (GL) scheme. Thus, given a mesh $t_j = j\tau$, $j = 0, 1, \ldots$, with constant step–size $\tau > 0$, the fractional time–derivative in the momentum equation of (14) is approximated as

$$\frac{\partial^\beta}{\partial t^\beta} u(t_n, x) \approx \frac{1}{\tau^\beta} \left[ u(t_n, x) + \sum_{j=0}^{n-1} \omega_{n-j}^{(\beta)} u(t_j, x) \right] \tag{27}$$

where $\omega_j^{(\beta)}$, $j = 0, 1, \ldots$, are the coefficients of the GL scheme which, for practical purposes, are evaluated by the recursion

$$\omega_0^{(\beta)} = 1, \quad \omega_j^{(\beta)} = \left( 1 - \frac{\beta + 1}{j} \right) \omega_{j-1}^{(\beta)},$$

and, in the same way, we discretize the time–fractional derivative in the continuity equation (14). Hence we create a mixed implicit/explicit scheme, in order to balance stability requirements with computational complexity, by imposing the momentum equation at the distinct times $t = t_n$ and $t = t_{n-1}$, namely

$$\frac{\partial^\beta}{\partial t^\beta} u(t_n, x) + \frac{1}{\rho_0} \frac{\partial p}{\partial x} p(t_n, x) = \nu \frac{\partial^2 u}{\partial x^2}(t_{n-1}, x),$$

and, after denoting for shortness the time-memory term with

$$F(t_{n-1}, x) = -\frac{1}{\tau^\beta} \sum_{j=0}^{n-1} \omega_{n-j}^{(\beta)} u(t_j, x) + \nu \frac{\partial^2}{\partial x^2} u(t_{n-1}, x), \tag{28}$$

and inserting the obtained discretized version of the velocity in the continuity equation, the system (14) is discretized, w.r.t. time, according to

$$\begin{cases} u(t_n, x) \approx \tau^\beta F(t_{n-1}, x) - \dfrac{\tau^\beta}{\rho} \dfrac{\partial}{\partial x} p(t_n, x) \\ p(t_n, x) \approx c^2 \tau^{\alpha+\beta} \dfrac{\partial^2}{\partial x^2} p(t_n, x) - \displaystyle\sum_{j=0}^{n-1} \omega_{n-j}^{(\alpha)} p(t_j, x) - c^2 \rho \tau^{\alpha+\beta} \dfrac{\partial}{\partial x} F(t_{n-1}, x). \end{cases}$$

For spatial derivatives, a special attention must be paid to prevent the introduction of spurious oscillations. A common technique in the numerical treatment of Navier-Stokes equations makes use of staggered grids where pressure is sought at the center and velocity on the faces of each cell. Thus, on a mesh $x_k = hk$, $k = 0, 1, \dots, M$, with constant width $h = L/M$ ($L > 0$ is the length of the domain), pressure values are considered at $x_k$ while the velocity is instead imposed at the mid-points $x_{k+\frac{1}{2}} = (x_k + x_{k+1})/2$, as depicted in Fig. 4 where balls and crosses denote pressure and velocity approximations, respectively. Second-order approximations give

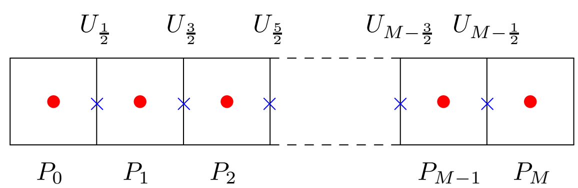


Figure 4: Representation of the spatial discretization of pressure $P$ (ball symbol) and velocity $U$ (cross symbol) on the staggered grid

$$
\begin{aligned}
&\frac{\partial}{\partial x}u(t,x_k) = \frac{1}{h}\Big(u(t,x_{k+\frac{1}{2}}) - u(t,x_{k-\frac{1}{2}})\Big) + \mathcal{O}\big(h^2\big)\\
&\frac{\partial}{\partial x}p(t,x_{k+\frac{1}{2}}) = \frac{1}{h}\Big(p(t,x_{k+1}) - p(t,x_k)\Big) + \mathcal{O}\big(h^2\big)\\
&\frac{\partial^2}{\partial x^2}u(t,x_{k+\frac{1}{2}}) = \frac{1}{h^2}\Big(u(t,x_{k+\frac{3}{2}}) - 2u(t,x_{k+\frac{1}{2}}) + u(t,x_{k-\frac{1}{2}})\Big) + \mathcal{O}\big(h^2\big)
\end{aligned}
$$

and, denoted with $U^n_{k+\frac{1}{2}}$, $F^n_{k+\frac{1}{2}}$ and $P^n_k$ the approximations of $u(t_n,x_{k+\frac{1}{2}})$, $F(t_n,x_{k+\frac{1}{2}})$ and $p(t_n,x_k)$ respectively, the fully discretized version of (14) is hence given by

$$
\begin{cases}
U^n_{k+\frac{1}{2}} = \tau^\beta F^{n-1}_{k+\frac{1}{2}} - L_1\left(P^n_{k+1} - P^n_k\right)\\
P^n_k = L_2\left(P^n_{k-1} - 2P^n_k + P^n_{k+1}\right) - \sum_{j=0}^{n-1}\omega^{(\alpha)}_{n-j}P^j_k - L_3\left(F^{n-1}_{k+\frac{1}{2}} - F^{n-1}_{k-\frac{1}{2}}\right)\\
F^{n-1}_{k+\frac{1}{2}} = \dfrac{R}{h^2}\left(U^{n-1}_{k+\frac{3}{2}} - 2U^{n-1}_{k+\frac{1}{2}} + U^{n-1}_{k-\frac{1}{2}}\right) - \dfrac{1}{\tau^\beta}\sum_{j=0}^{n-1}\omega^{(\beta)}_{n-j}U^j_{k+\frac{1}{2}}
\end{cases}
$$

which applies on internal nodes only, namely when $k = 1,\dots,M-2$ for $U^n_{k+\frac{1}{2}}$ and $F^n_{k+\frac{1}{2}}$ and when $k = 1,\dots,M-1$ for $P^n_k$. The following constants have beein introduced for easy of presentation

$$
L_1 = \frac{\tau^\beta}{\rho h},\quad L_2 = \frac{c^2\tau^{\alpha+\beta}}{h^2},\quad L_3 = \frac{c^2\rho\tau^{\alpha+\beta}}{h}. \tag{29}
$$

For convenience vector notations $\bar{U}^n = \big(U^n_{\frac{1}{2}}, U^n_{\frac{3}{2}},\dots,U^n_{M-\frac{1}{2}}\big)^T \in \mathbb{R}^M$, $\bar{F}^n = \big(F^n_{\frac{1}{2}}, F^n_{\frac{3}{2}},\dots,F^n_{M-\frac{1}{2}}\big)^T \in \mathbb{R}^M$ and $\bar{P}^n = \big(P^n_1, P^n_2,\dots,P^n_{M-1}\big)^T \in \mathbb{R}^{M-1}$ are introduced. To obtain the approximation of the boundary values $F_{\frac{1}{2}}^{n-1}$ and $F_{M-\frac{1}{2}}^{n-1}$, we impose outflow conditions such that the following fictitious external boundary conditions $U_{-\frac{1}{2}}^{n} = U_{\frac{1}{2}}^{n}$ and $U_{M+\frac{1}{2}}^{n} = U_{M-\frac{1}{2}}^{n}$ are obtained for the velocity component. In this way, we are able to evaluate

$$\bar{F}^{n-1} = \frac{R}{h^2} A_{22} \bar{U}^{n-1} - \frac{1}{\tau^\beta} \sum_{j=0}^{n-1} \omega_{n-j}^{(\beta)} \bar{U}^j \tag{30}$$

and hence

$$\begin{aligned} \bar{U}^n &= \frac{\tau^\beta R}{h^2} A_{22} \bar{U}^n - \sum_{j=0}^{n-1} \omega_{n-j}^{(\beta)} \bar{U}^j - L_1 A_{21} \bar{P}^n \\ \bar{P}^n &= L_2 A_{11} \bar{P}^n - \sum_{j=0}^{n-1} \omega_{n-j}^{(\alpha)} \bar{P}^j - L_3 A_{12} \bar{F}^{n-1} + L_2 \hat{P}^n \end{aligned} \tag{31}$$

with $A_{11} \in \mathbb{R}^{(M-1)\times(M-1)}$, $A_{22} \in \mathbb{R}^{M\times M}$ being the matrices derived from the 3-point stencils $(1, -2, 1)$ approximating $\partial^2/\partial x^2$ and $A_{12} \in \mathbb{R}^{(M-1)\times M}$, $A_{21} \in \mathbb{R}^{M\times(M-1)}$ the matrices derived from the 2-point stencils $(1, -1)$ approximating $\partial/\partial x$. A straightforward rearrangement of the above equations finally leads to

$$\left\{ \begin{aligned} \big(I - L_2 A_{11}\big) \bar{P}^n &= -\sum_{j=0}^{n-1} \omega_{n-j}^{(\alpha)} \bar{P}^j - L_3 A_{12} \bar{F}^{n-1} + L_2 \hat{P}^n \\ \big(I - \frac{\tau^\beta R}{h^2} A_{22}\big) \bar{U}^n &= -\sum_{j=0}^{n-1} \omega_{n-j}^{(\beta)} \bar{U}^j - L_1 A_{21} \bar{P}^n - L_1 \tilde{P}^n \end{aligned} \right. \tag{32}$$

with $\hat{P}^n = \big(p_{in}, 0, \ldots, 0, p_{out}\big)^T \in \mathbb{R}^{M-1}$, $\tilde{P}^n = \big(-p_{in}, 0, \ldots, 0, p_{out}\big)^T \in \mathbb{R}^M$ and where pressure values $p_{in} = P_{CR}(t_n)$ and $p_{out} = P_{AV}(t_n)$ in the common rail and in the accumulation volume are introduced from the available data.

Since the presence of a persistent memory-term, which makes the computation extremely demanding, we adopt a short-memory approach by truncating the memory and including just the last $500$ instances, an approach which does not affect in a significant way the accuracy of the solutions.

## 6. Parametric Optimization by Differential Evolution

The mechanical parameters of the dynamical model and the fractional orders are now optimized to improve the model prediction capability for the main output variable, i.e. the fuel injection flowrate. The elastic constants of the mass-spring-damper model and the fractional orders are optimized to provide the optimal fit to an experimental flowrate, so that the model well adheres to the real deformation and displacement of the plunger-needle coupling and to the flow in the high pressure pipe. Table 1 shows the initial values of the parameters denoted by $x_{i,ref}$, with $i = 1, \ldots, 7$ and provided by geometric dimensions and Young's modulus. These values and $\alpha = \beta = 1$ are used to start the optimization.

The problem is formalized as follows:

$$\underset{\mathbf{x} \in X}{min} \left\{ J(\mathbf{x}) \in \mathbb{R} \middle| \mathbf{q}(\mathbf{x}) > \mathbf{0}, \mathbf{h}(\mathbf{x}) \geq \mathbf{0}, \mathbf{g}(\mathbf{x}) \geq \mathbf{0}, \mathbf{f}(\mathbf{x}) \geq \mathbf{0} \right\}, \tag{33}$$

where $J(\mathbf{x})$ is an objective function that quantifies the model prediction accuracy, and $\mathbf{q}(\mathbf{x})$, $\mathbf{h}(\mathbf{x}) = [h_1(\mathbf{x}), h_2(\mathbf{x}), \ldots, h_{14}(\mathbf{x})]$, $\mathbf{g}(\mathbf{x})$ and $\mathbf{f}(\mathbf{x})$ are the constraints, defined in Table 2. The optimization is based on experimental data obtained from a test bench: the EVI (injection curve indicator) profile is the reference, representing the injection flowrate as a function of time, when the electro-injector is driven by a pre-defined current. Then

$$J(\mathbf{x}) = \sum_{t_k} |y_{mod}(t_k, \mathbf{x}) - y_{exp}(t_k)| \tag{34}$$

where $y_{exp}(t_k)$ is the experimental value and $y_{mod}(t_k, \mathbf{x})$ is the model predicted value at sampling time $t_k$.

The constraints on $k_i$ express physical limitations to obtain feasible values of the optimized parameters, then they limit the space of possible solutions to the optimization.

Table 2: Constraints

| Constraint | Expression |
| --- | --- |
| $\mathbf{q}(\mathbf{x})$ | $\mathbf{A} \cdot \mathbf{x} > 0$ |
| $h_i(\mathbf{x})$ | $k_i - \left(1 - \frac{\alpha_{i,min}}{100}\right) k_{i,ref} \geq 0,\ i = 1, \ldots, 7$ |
| $h_{i+7}(\mathbf{x})$ | $\left(1 + \frac{\alpha_{i,max}}{100}\right) k_{i,ref} - k_i \geq 0,\ i = 1, \ldots, 7$ |
| $g_1(\mathbf{x})$ | $\alpha > 0$ |
| $g_2(\mathbf{x})$ | $1 - \alpha > 0$ |
| $g_3(\mathbf{x})$ | $\beta > 0$ |
| $g_4(\mathbf{x})$ | $1 - \beta > 0$ |
| $f_1(\mathbf{x})$ | $\alpha - \left(1 - \frac{pv_1}{100}\right) \alpha_{ref} > 0$ |
| $f_2(\mathbf{x})$ | $\left(1 + \frac{pv_2}{100}\right) \alpha_{ref} - \alpha > 0$ |
| $f_3(\mathbf{x})$ | $\beta - \left(1 - \frac{pv_1}{100}\right) \beta_{ref} > 0$ |
| $f_4(\mathbf{x})$ | $\left(1 + \frac{pv_2}{100}\right) \beta_{ref} - \beta > 0$ |

Some constraints come from the geometrical and physical differences among cylindrical components of the plunger and needle. Namely, they are characterized by different sections and lengths. For example, for the needle, since the cylinder of mass $m_7$ has a greater stiffness than the cylinder of mass $m_6$, the inequality $k_7 < k_6$ must be enforced. The complete mechanical coupling should satisfy the inequalities

$$k_7 < k_2 < k_3 < k_5 < k_4 < k_1 < k_6, \tag{35}$$

which are written as $k_7 - k_2 < 0$, $k_2 - k_3 < 0$, $k_3 - k_5 < 0$, $k_5 - k_4 < 0$, $k_4 - k_1 < 0$, $k_1 - k_6 < 0$. These six linear inequality constraints on the first seven decision variables can be expressed by $\mathbf{q}(\mathbf{x}) = \mathbf{A} \cdot \mathbf{x} > 0$ (see Table 2), where $\mathbf{x} = [k_1\ k_2\ k_3\ k_4\ k_5\ k_6\ k_7\ \alpha\ \beta]^T$, and $\mathbf{A}$ is easily obtained.

Some other constraints depend on the maximum variation allowed for each parameter $k_i$, whose nominal value is $k_{i,ref}$. Each parameter must stay within the percentage range of $\left[\left(1-\frac{\alpha_{i,min}}{100}\right)k_{i,ref}, \left(1+\frac{\alpha_{i,max}}{100}\right)k_{i,ref}\right]$ around $k_{i,ref}$, where $\alpha_{i,min}$ and $\alpha_{i,max} \in [0,100]$ are fixed at the beginning of the optimization. Then, two inequalities hold for each $k_i$, $i = 1, \dots, 7$ to specify upper and lower bounds, respectively, resulting in $14$ inequality constraints:

$$\begin{cases} h_i(\mathbf{x}) = x_i - \left(1 - \dfrac{\alpha_{i,min}}{100}\right) x_{i,ref} \geq 0 \\ h_{i+n_p}(\mathbf{x}) = \left(1 + \dfrac{\alpha_{i,max}}{100}\right) x_{i,ref} - x_i \geq 0 \end{cases} \tag{36}$$

The constraints in $\mathbf{g}(\mathbf{x}) > 0$ define the limits of the fractional orders (see Table 2). The constraints in $\mathbf{f}(\mathbf{x}) > 0$ depend on the maximum variations of $\alpha$ and $\beta$, which are inside $\left[\left(1-\frac{pv_1}{100}\right)\alpha_{ref}, \left(1+\frac{pv_2}{100}\right)\alpha_{ref}\right]$ and $\left[\left(1-\frac{pv_1}{100}\right)\beta_{ref}, \left(1+\frac{pv_2}{100}\right)\beta_{ref}\right]$, with $pv_1$ and $pv_2$ fixed percentage variations.

Intelligent parameter optimization regards finding $\mathbf{x}^*$ such that $J(\mathbf{x}^*) \leq J(\mathbf{x})$ for every $\mathbf{x} \in S$, where $S$ is the search space. Analytical solutions are not possible because $J$ is not continuous and not differentiable, because of the nonlinearity of the problem and the number of parameters, etc. Then heuristic and stochastic search are often employed [9].

We selected differential evolution (DE) to solve the considered optimization problem. DE has been widely used in many applications because of its implicity and efficiency. Further, it requires tuning of few algorithmic parameters [31, 35, 27, 8, 6]. In the considered problem, DE can be very useful to save time and costs in developing the prototype solution for the mechanical layout of the injector. Moreover, DE is often more effective than other meta-heuristic optimization techniques in finding the optimum solutions for given time and computation constraints. Benchmark problems showed that DE is usually superior in optimization and in robustness to different initial conditions [35]. For details on the algorithm implementation, refer to [31].

## 7. Simulation Results

A simulation model was developed by taking into account all the details of the mathematical model previously described and the numerical approach of the previous section by a specific Matlab code. To simplify the model, a constant section is assumed along the whole length of the high pressure pipe. In this way, the water hammer effect and abrupt pressure changes from one section to another can be neglected. Moreover, the number of spatial discretization points is $20 \leq M \leq 100$ (increasing $M$ improves the accuracy but requires a smaller time step) and the number of time discretization points is $3000 \leq N \leq 10000$ (increasing $N$ improves the accuracy but also the computation time). Then, for the considered simulation interval $[0, 1.6]$ ms, $\tau \in [10^{-4}, 10^{-3}]$ ms provides good accuracy. Finally, the CR pressure experimental values are used as input pressures to the pipe.

The simulation objective is to predict the fuel flowrate that is injected into the cylinder (output from the SAC volume in Fig. 2), which gives a time behavior usually termed as EVI profile. The result is compared with experimental data available from a real electro-injector. The injected flowrate is measured by a Bosch Rate of Injection Meter [3]. In particular, data were collected in typical working conditions: a CR reference pressure of 800/1200/1600 bar, the injectors excitation time interval of $700\,\mu$s, a sampling period of $10\,\mu$s.

The Simulink block diagram used for simulation is shown in Fig. 5. The pipe block includes the fractional-order model of wave pressure propagation. The valve block includes the electrical model and the mechanical model of the shutter. The plunger-needle block represents the series of spring-mass-damper elements. The control chamber, the SAC and accumulation volumes employ the classical continuity and momentum equations to find pressures and flowrates. Note that boundary conditions necessary to solve the equations are specified by the valve command $V_{ref}$, the measured pressure in the common rail $P_{CR}$, the measured pressure $P_{low}$ in the low pressure circuit, the measured pressure $P_{cyl}$ in the cylinder. The output block gives the injected flowrate.

Optimization is achieved after two steps. The first uses 120 flowrate experimental values, characterized by a sampling period of $10\,\mu$s. The second step employs two other sets of 120 data and is necessary to validate the results. The three experiments were made at different rail pressures (1600, 1200 and 800 bar).

Each iteration provides the best solution according to the minimization of $J$. The last generation provides the best solution associated to the global minimum of $J$. The DE parameters are set empirically: the number of candidate solutions is varied starting with $N_{pop} = 90$ because a rule of thumb indicates ten times the dimensionality of the problem $(10 \cdot 9)$ to avoid premature convergence or stagnation [31]. The number of generations, $G_{max}$, is changed until a low global minimum of $J$ is obtained. Best results are obtained with $N_{pop} = 60$ and $G_{max} = 70$.

Fig. 6 shows the objective function in the first step ($p_{CR} = 1600$ bar): the best and mean values are plotted for each generation. Different values of $G_{max}$ and $N_{pop}$ yield higher errors in the validation step (with $p_{CR} = 1200$ or $800$ bar).

Now the prediction by the fractional-order optimized model is compared to:

- the nominal model not subject to optimization;

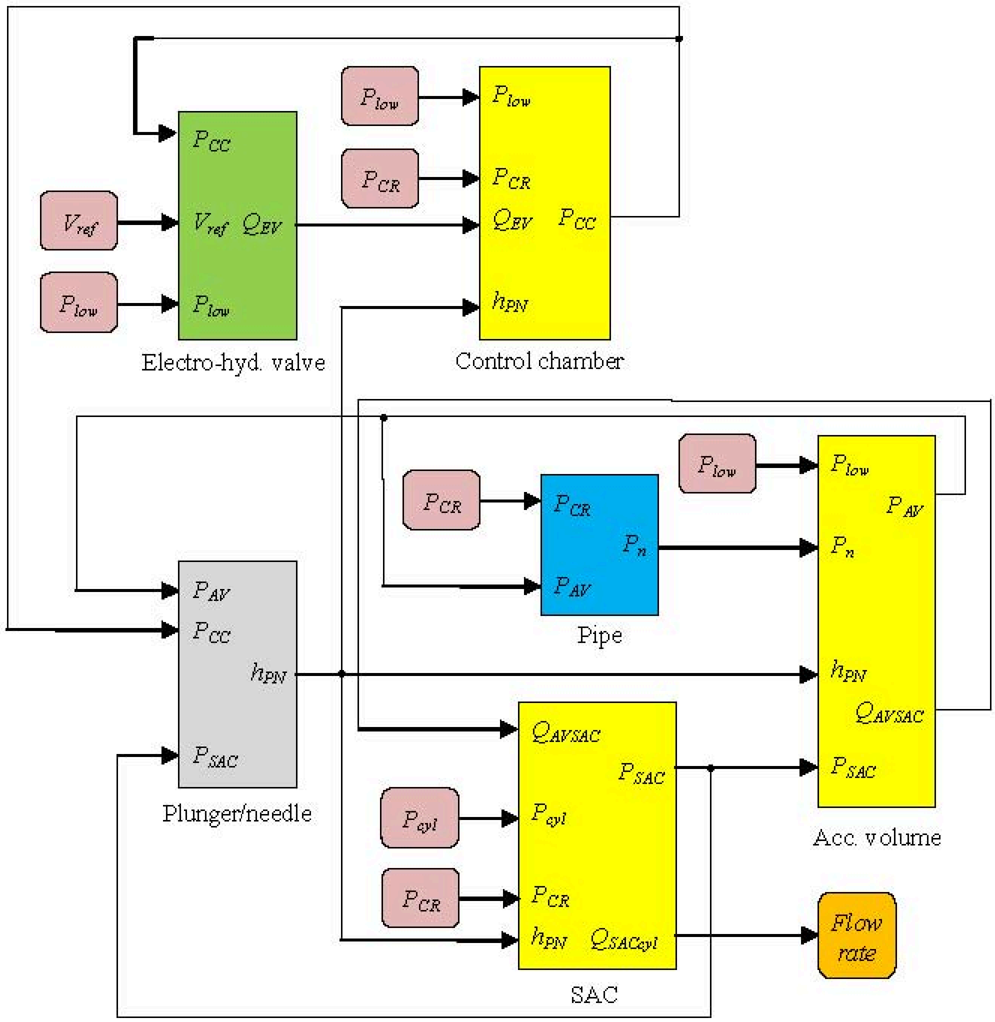


Figure 5: Simulink block diagram for simulation

- the model considering the plunger-needle as a unique rigid body, which can not describe deformation by the pressure forces [28];

- the optimized integer-order model.

Fig. 7 shows the results from the first step. Figures 8-9 show the prediction

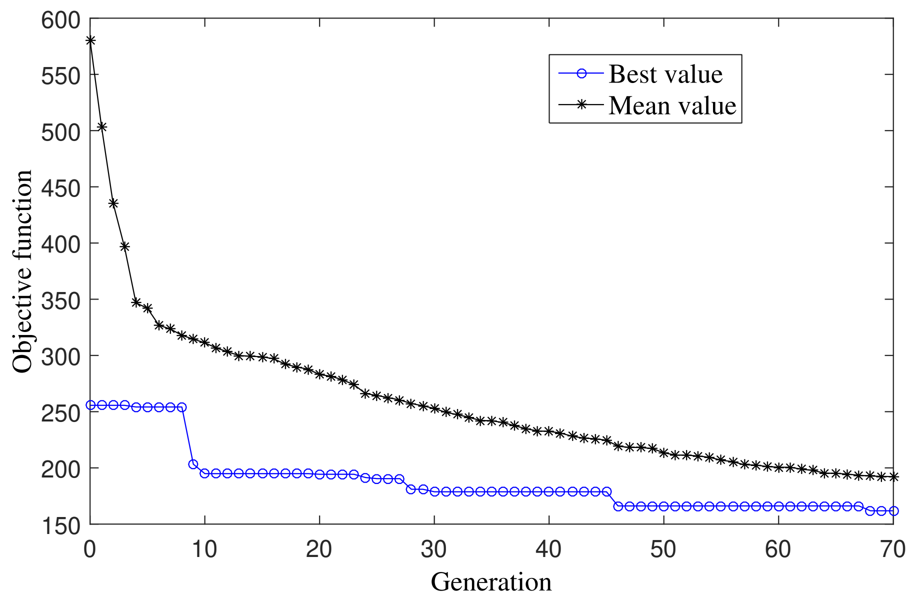


Figure 6: Evolution of the optimization index $J$

in the validation step. Experimental data are shown by dashed lines. The results by the optimized fractional-order model, the optimized integer-order model, the nominal model, and the rigid body model are indicated by solid blue, dashed light-blue, green, and red lines, respectively.

The rigid body model is clearly outperformed (see much higher errors and delay in the response), because it disregarded the deformation of the mechanical coupling. It is less prompt than a nominal/optimized model, which includes the mass elements for representing the reaction to pressure variations in the adjacent volumes.

In general, injection can be roughly divided in three phases: a fast-rising flowrate, a saturation or slow increase, and a rapid fall. If the model predicts a

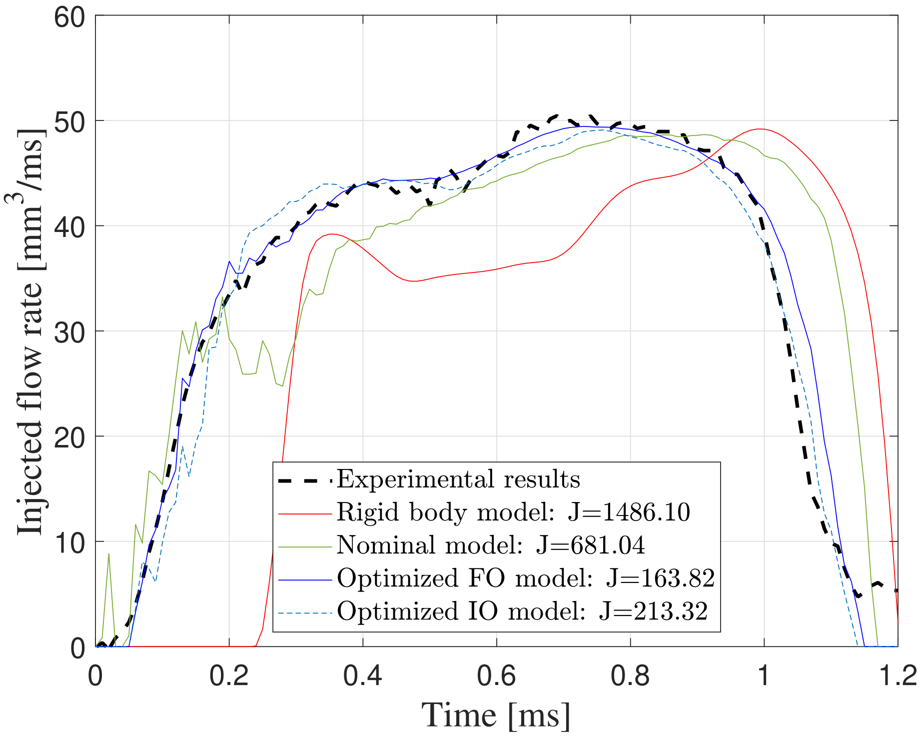


Figure 7: Prediction of the flowrate with $p_{CR} = 1600$ bar

delayed start or finish of the injection, then it is unreliable. Namely, the start and finish affect the combustion efficiency and emissions. So, it is important to correctly estimate the duration and trend of the flowrate.

In the case of $1600$ bar, the nominal model shows higher errors than the optimized model, especially starting from the end of the first phase on (for $t \geq 0.2$ ms). In the validation with $1200$ or $800$ bar, the nominal model shows a similar trend with errors that are even higher. The optimized integer-order model (dashed light blue line) provides a worst fitting to experimental data than the optimized fractional order model. In synthesis, the prediction by the optimized fractional-

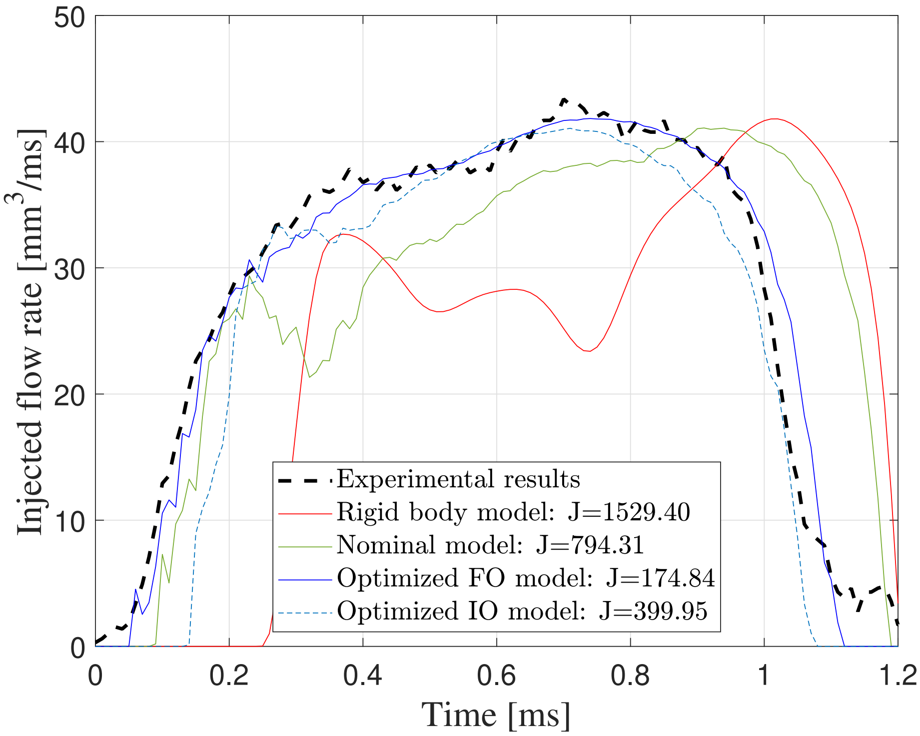


Figure 8: Prediction of the flowrate with $p_{CR} = 1200$ bar

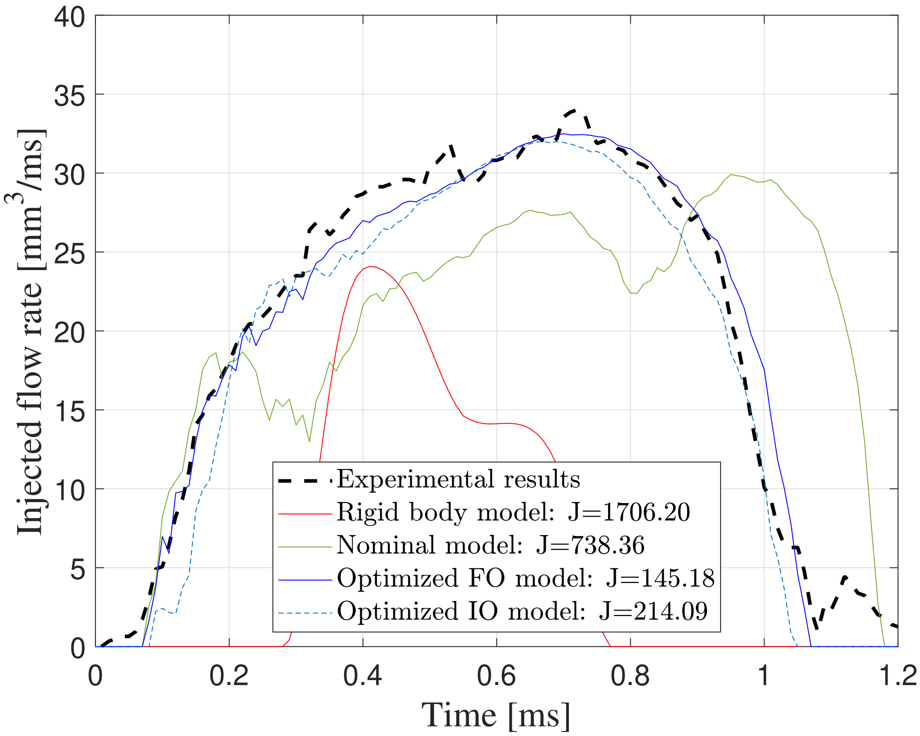


Figure 9: Prediction of the flowrate with $p_{CR} = 800$ bar

order model is better in all cases and a very good match between simulation results and experimental data can be observed.

## 8. Conclusion

Although automotive companies are more and more investing in electric and hybrid engines, production and sales of engines based on Diesel common rail technology still takes a high share of the market. To adhere to strict regulations and limit polluting emissions, industry and academic research are much focused on improving the Diesel CR technology. In particular, the performance of the

Diesel CR injection system strongly depends on the employed electro-injectors, a small yet important component. This work introduced a new mathematical representation of the fuel dynamics in an advanced injector, namely in a specific pipe that delivers fuel arriving from the common rail volume to the terminal volume which accumulates fuel before injection. The injector and the pipe inside it show a complex fluid dynamics, in particular a high-pressure flow according to a sort of wave propagation in the pipe.

The mathematical model describes the fuel flow, the internal decomposition of the injector into control volumes and mechanical elements subject to deformation, the electromagnetic valve for flow regulation, and, above all, the fuel dynamics inside the mentioned pipe. To this last purpose, partial differential equations with fractional-order time derivatives are used. They are obtained by starting from classical integer-order continuity and momentum equations. Conservation laws are however not violated thanks to a physical interpretation based on the fact that the injector is not a closed system, hence it loses energy (fractional mass conservation is justified), and on the usage of fractional viscosity (for a fractional momentum balance).

The fractional-order model is numerically solved by time and space discretization. The parameters of the model are optimized by a differential evolution technique that minimizes the prediction error on the main performance index, the injected flowrate. The optimized model shows several nice properties tested by simulation. First, it matches experimental data obtained from a real electro-injector. Second, it predicts the injected flowrate in distinct working conditions. Then, it can be useful for design and optimization of the injector layout and parameters. Finally, it can be used for model-based control of fuel injection.

## Acknowledgment

This paper is based upon work from COST Action CA15225, a network supported by COST (European Cooperation in Science and Technology).

## References

[1] Anandan S., Gagliano S., Bucolo M. (2015). Computational models in microfluidic bubble logic. *Microfluidics and Nanofluidics* 18 (2), pp. 305–321.

[2] Bai Y., Lan Q., Fan L., Ma X., Liu H. (2021). nvestigation on the fuel injection stability of high pressure common rail system for diesel engines. *International Journal of Engine Research* 22 (2), pp. 616–631.

[3] Bower G. R., Foster D. E. (1991).A comparison of the Bosch and Zuech rate of injection meters. SAE Paper 910724.

[4] Cairone F., Anandan P., Bucolo M. (2018). Nonlinear systems synchronization for modeling two-phase microfluidics flows. *Nonlinear Dynamics* 92 (1), pp. 75–84.

[5] Cairone F., Gagliano S., Carbone D. C., Recca G., Bucolo M. (2016). Micro-optofluidic switch realized by 3D printing technology. *Microfluidics and Nanofluidics* 20 (4), 61.

[6] Chakraborty U. (2008). *Advances in Differential Evolution*, Springer-Verlag, Berlin.

[7] Colin G., Lanusse P., Louzimi A., Chamaillard Y., Deng C., Nelson-Gruel D. (2011). Multi-SISO robust CRONE design for the air path control of a

diesel engine, in S. Bittanti, A. Cenedese, and S. Zampieri (eds.), Proc. 18th IFAC World Congress, Milan, Italy, 28 Aug. - 2 Sep., 2011, vol. 18, Part 1, pp. 2254–2259.

[8] Das S., Konar A., Chakraborty U. (2005). Two Improved Differential Evolution Schemes for Faster Global Search, 7th Annual Conference on Genetic and Evolutionary Computation, H. Beyer (Ed.), Washington, DC, June 25–29, ACM-SIGEVO, pp. 991–998.

[9] Dellino G., Lino P., Meloni C., Rizzo A. (2007). Enhanced evolutionary algorithms for multidisciplinary design optimization: A control engineering perspective, In: *Hybrid Evolutionary Algorithms* (Studies in Computational Intelligence, Vol. 79), Grosan C., Abraham A., Ishibuchi H. (Eds.), Springer, Heidelberg, pp. 39–76.

[10] Dongiovanni C., Coppo M. (2010). Accurate modelling of an injector for common rail systems. In D. Siano (Ed.), *Fuel Injection*, Sciyo (HRV), Rejeka, pp. 95–119.

[11] Dyntar D., Onder C., Guzzella L. (2002). Modeling and control of CNG engines. SAE Paper No. 2002-01-1295.

[12] Gagliano S., Cairone F., Amenta A., Bucolo M. (2019) A Real Time Feed Forward Control of Slug Flow in Microchannels, *Energies* 12 (13), 2556.

[13] Gagliano S., Stella G., Bucolo M. (2020) Real-time Detection of Slug Velocity in Microchannels, *Micromachines* 11 (3), 241.

[14] Garrappa R., Lino P., Maione G., Saponaro F. (2015). Modeling and Numerical Analysis of Fractional-Order Dynamics in Electro-injectors Pipes. 2015

54th IEEE Conference on Decision and Control (CDC), Osaka, Japan, 15-18 Dec. 2015, pp. 5984–5989.

[15] Guzzella L. (2009). The Automobile of the Future – Options for Efficient Individual Mobility. 3rd IEEE Multiconference on Systems and Control, Saint Petersburg, Russia, July 8–10, pp. i-i.

[16] Holm, S. (2019). *Waves with Power-Law Attenuation*. Springer and ASA Press, Switzerland.

[17] Holm S., Sinkus R. (2010). A unifying fractional wave equation for compressional and shear waves. *J. Acoust. Soc. Am.*, 127:542–548.

[18] Kapetina M. N., Lino P., Maione G., Rapaic M. R. (2017). Estimation of non-integer order models to represent the pressure dynamics in common-rail natural gas engines. 20th IFAC World Congress 2017, Toulouse, France, July 9-14, IFAC-PapersOnLine, vol. 50, issue 1, July 2017, pp. 14551–14556.

[19] Lino P., Maione B., Amorese C. (2008). Modelling and predictive control of a new injection system for compressed natural gas engines. *Control Engineering Practice*, vol. 16, 10, pp. 1216–1230.

[20] Lino P., Maione B., Rizzo A. (2005). A Control-Oriented Model of a Common Rail Injection System for Diesel Engines, 10th IEEE Conference on Emerging Technologies and Factory Automation (ETFA 2005), Catania, Italy, Sept. 19–22, Vol. 1, pp. 557–563.

[21] Lino P., Maione G. (2013). Fractional order control of the injection system in a CNG engine. 12th European Control Conference (ECC 2013), Zürich, Switzerland, July 17-19, pp. 3997–4002.

[22] Lino P., Maione G. (2013). Design and simulation of fractional-order controllers of injection in CNG engines, in T. Kawabe (ed.), 7th IFAC Symposium on Advances in Automotive Control (AAC 2013), Tokyo, Japan, Sep. 4-7, vol. 7, Part 1, pp. 582–587.

[23] Lino P., Maione G. (2014). Switching fractional-order controllers of common rail pressure in compressed natural gas engines, Proceedings of the 19th IFAC World Congress, Cape Town, South Africa, Aug. 24-29, pp. 2915–2920.

[24] Lino P., Maione G., Saponaro F., Li K. (2014). Evolutionary Parameter Optimization of Electro-Injector Models for Common Rail Diesel Engines, in *Intelligent Computing in Smart Grid and Electrical Vehicles* (Communications in Computer and Information Science, Vol. 463), K. Li, Y. Xue, S. Cui, Q. Niu (Eds.), Springer-Verlag, Berlin, pp. 539–551.

[25] Mohebbi M., Aziz A. A., Hamidi A., Hajialimohammadi A., Hosseini V. (2016). Modeling of pressure line behavior of a common rail diesel engine due to injection and fuel variation. *Journal of the Brazilian Society of Mechanical Sciences and Engineering* 39 (3), pp. 661–669.

[26] Moze M., Sabatier J., Oustaloup A. (2010). Air-fuel ratio control of an internal combustion engine using CRONE control extended to LPV systems, in *New Trends in Nanotechnology and Fractional Calculus Applications*, vol. 2, D. Baleanu, Z. B. Guvenc, J. A. Tenreiro Machado, Eds. Dordrecht: Springer, 2010, pp. 71–86.

[27] Price K., Storn R., Lampinen J. (2005). *Differential Evolution – A Practical Approach to Global Optimization*, Springer, Berlin.

[28] Saponaro F., Lino P., Maione G. (2014). A dynamical model of electro-injectors for common rail diesel engines, 2014 22nd Mediterran. Conf. on Control & Automation (MED'14), Palermo, Italy, June 16-19, pp. 207–211.

[29] Sapuppo F., Schembri F., Fortuna L., Llobera A., Bucolo M. (2012). A polymeric micro-optical system for the spatial monitoring in two-phase microfluidics. *Microfluidics and Nanofluidics*, 12(1-4), pp. 165–174.

[30] Stokes G. G. (1845). On the theories of the internal friction of fluids in motion, and of the equilibrium and motion of elastic solids. *Trans. Cambridge Philos. Soc.*, vol. 8 (part III), pp. 287–319.

[31] Storn R., Price, K. (1997). Differential Evolution: A Simple and Efficient Heuristic for Global Optimization Over Continuous Spaces. *J. Global Optim.*, 11(4), pp. 341–359.

[32] Streeter V., Wylie K., Bedford E. (1988). *Fluid Mechanics*, 9th ed., McGraw-Hill, New York.

[33] Stumpp G., Ricco M. (1996). Common rail – An attractive fuel injection system for passenger car DI diesel engine. SAE Technical Paper, 960870, pp. 181–191.

[34] Uchaikin V. V. (2013). *Fractional Derivatives for Physicists and Engineers: Volume I Background and Theory*. Springer, Berlin Heidelberg.

[35] Vesterstrøm J., Thomsen R. (2004). A Comparative Study of Differential Evolution, Particle Swarm Optimization, and Evolutionary Algorithms on Numerical Benchmark Problems, Congress on Evolutionary Computation (CEC2004), Portland, OR, June 19-23, Vol. 2, pp. 1980–1987.

[36] Yan F., Chen S., Zeng X., Zhao J., Wang J. (2013). Modeling and analysis of fuel injection split for Diesel engine active fueling control. *ASME J. Dyn. Syst., Meas., Control*, 135 (6), p. 061016.